Electrical spin injection and accumulation at room temperature in an all-metal mesoscopic spin valve

Jedema, F.J.; Filip, A.T.; Wees, B.J. van

Published in:
Physica E: Low-dimensional Systems and Nanostructures

Publication date:
2001

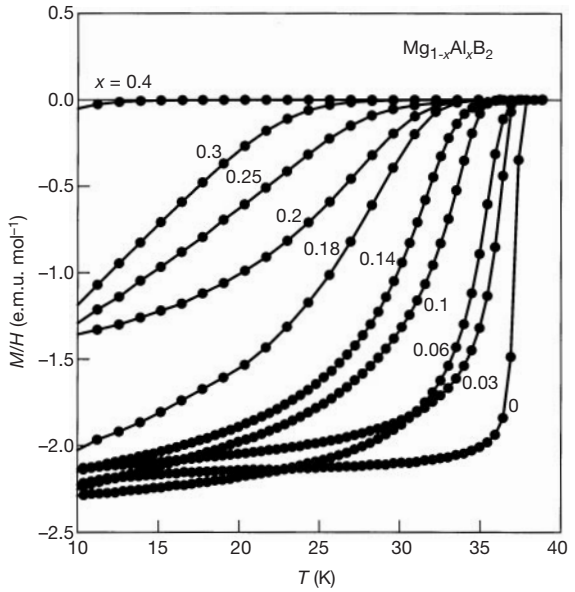

Figure 3 Magnetization of $Mg_{1-x}Al_xB_2$ as a function of temperature and Al concentration. The figure shows magnetic characterization of the superconducting transitions for polycrystalline powders of $Mg_{1-x}Al_xB_2$ for $x = 0$–0.40. A field of 15 Oe was applied after cooling the samples in zero field.

The onsets of the transitions are all in the vicinity of 36 K, the transition temperature for $x = 0.10$. There is no bulk superconducting transition for $x = 0.3$ and $x = 0.4$. The data are interpreted as indicating that bulk superconductivity in single-phase material is suppressed for x greater than 0.10. The superconducting transitions observed in the two-phase region are due to both the decreasing amount of the bulk superconducting phase with increasing Al content, and also to the distribution of Al contents in the powders. The structural and magnetic data taken together therefore indicate that the disappearance of bulk superconductivity in $Mg_{1-x}Al_xB_2$ occurs at the same Al concentrations at which a structural transition occurs—this transition results in the partial collapse of the separation between boron planes.

The similarity of the calculated electronic density of states (DOS) for MgB_2 and AlB_2 (ref. 6) indicates that the effect of substituting Al for Mg can be considered primarily as a simple filling of available electronic states, with one electron donated per Al, within a 'rigid band' picture. The calculations show[4–6] that there is a sharp drop in the DOS of MgB_2 at only slightly higher electron concentrations. The gradual decrease of T_c from 38 to 36 K with increasing Al content in the single-phase region below $x = 0.1$ may therefore be due to the expected decrease of the DOS at E_F with increasing electron count, consistent with a conventional origin for the superconductivity[10].

High-resolution structural study of uniform powders, if they prove possible to synthesize, would help to determine how the superconductivity and the structural transition are linked on an electronic level. The proximity of MgB_2 to a structural instability is consistent with a general picture for conventional high-temperature superconductors as being near chemical phase instability owing to strong electron–lattice coupling. However, our data for $Mg_{1-x}Al_xB_2$ do not suggest that the structural instability in this case is driven by competition between superconductivity and a structural distortion that would decrease the density of electronic states at the Fermi energy; this is because the Al substitution both decreases T_c and decreases the DOS at E_F before the transition occurs. It is at first sight surprising that the observed structural instability in MgB_2 involves a partial collapse of the separation of the boron layers, not a change in the boron–boron in-plane distance. It will be of interest to determine whether this collapse is associated with special characteristics of the electronic band filling near 0.1 excess electrons per cell. □

Received 8 February; accepted 16 February 2001.

1. Nagamatsu, J., Nakagawa, N., Muranaka, T., Zenitani, Y. & Akimitsu, J. Superconductivity at 39 K in magnesium diboride. *Nature* **410,** 63–64 (2001).
2. Jones, M. E. & Marsh, R. E. The preparation and structure of magnesium boride, MgB_2. *J. Am. Chem. Soc.* **76,** 1434–1436 (1954).
3. Killian, E. G. & Kaner, R. B. Synthesis of refractory ceramics via rapid metathesis reactions between solid-state precursors. *Chem. Mater.* **8,** 333–343 (1996).
4. Kortis, J., Mazin, I. I., Belaschenko, K. D., Antropov, V. P. & Boyer, L. L. Superconductivity of metallic boron in MgB_2. Preprint cond-mat/0101446 at ⟨http://xxx.lanl.gov⟩ (2001).
5. Armstrong, D. R. & Perkins, P. G. Electronic band structure of magnesium diboride. *J. Chem. Soc. Faraday Trans. 2* **75,** 12–16 (1979).
6. Ivanovskii, A. L. & Medvedeva, I. Interatomic interactions and electronic structure of hexagonal magnesium, aluminum and silicon diborides: Ab initio full-potential LMTO calculations. *Russ. J. Inorg. Chem.* **45,** 1234–1240 (2000).
7. Vekshina, N. V., Markovskii, L. Ya., Kondrashev, Yu. D. & Voevodskyaya, T. K. Binary borides of aluminum and magnesium. *Zh. Prikl. Khim.* **44,** 958–963 (1971).
8. Massalski, T. B. (ed.) *Binary Alloy Phase Diagrams* 498–499 (ASM International, Materials Park, Ohio, 1990).
9. Villars, P. & Calvert, L. D. *Pearson's Handbook of Crystallographic Data for Intermetallic Phases* 127–128 (ASM International, Materials Park, Ohio, 1991).
10. Bud'ko, S. L. *et al.* Boron isotope effect in superconducting MgB_2. Preprint cond-mat/0101463 at ⟨http://xxx.lanl.gov⟩ (2001).

Acknowledgements

This work was supported by the US Department of Energy and the National Science Foundation.

Correspondence and requests for materials should be addressed to R.J.C. (e-mail: rcava@princeton.edu).

Electrical spin injection and accumulation at room temperature in an all-metal mesoscopic spin valve

F. J. Jedema, A. T. Filip & B. J. van Wees

Department of Applied Physics and Materials Science Centre, University of Groningen, Nijenborgh 4.13, 9747 AG Groningen, The Netherlands

Finding a means to generate, control and use spin-polarized currents represents an important challenge for spin-based electronics[1–3], or 'spintronics'. Spin currents and the associated phenomenon of spin accumulation can be realized by driving a current from a ferromagnetic electrode into a non-magnetic metal or semiconductor. This was first demonstrated over 15 years ago in a spin injection experiment[4] on a single crystal aluminium bar at temperatures below 77 K. Recent experiments[5–8] have demonstrated successful optical detection of spin injection in semiconductors, using either optical injection by circularly polarized light or electrical injection from a magnetic semiconductor. However, it has not been possible to achieve fully electrical spin injection and detection at room temperature. Here we report room-temperature electrical injection and detection of spin currents and observe spin accumulation in an all-metal lateral mesoscopic spin valve, where ferromagnetic electrodes are used to drive a spin-polarized current into crossed copper strips. We anticipate that larger signals should be obtainable by optimizing the choice of materials and device geometry.

Spin accumulation plays an important role in spin-polarized

transport phenomena such as giant magnetoresistance (GMR), domain-wall magnetoresistance and spin-current-induced magnetization switching experiments[9–12]. We wanted to study the effect isolated from other spin-related phenomena, such as spin-dependent interface scattering, anisotropic magnetoresistance (AMR) and Hall effects. Large spin-accumulation effects have been claimed, using a ferromagnet–normal-metal–ferromagnet sandwich geometry[13,14]. However, the interpretation of the data has raised problems, because the magnitude of the observed effect requires a spin polarization of the current in the normal metal of around 100% (refs 15–18). Another problem is that the magnetoresistance effects of the ferromagnetic contacts, such as AMR and Hall effects, can mask or even mimic the spin-accumulation signal.

We have fabricated mesoscopic lateral spin valves to isolate the spin accumulation signal completely, using a multi-terminal geometry. In our spin-injection experiments, we use permalloy $Ni_{80}Fe_{20}$ (Py) electrodes to drive a spin-polarized current into copper (Cu) cross strips (Fig. 1). We observe clear spin valve signals at $T = 4.2$ K, as well as at room temperature. From our analysis we deduce a spin-flip length λ_N in the Cu wire of about 1 μm at 4.2 K, which is reduced to about 350 nm at room temperature.

Two batches of samples were made in a two-step lift-off process, using electron-beam lithography for patterning. The first batch (1) had a fixed Py electrode spacing L of 250 nm, and in the second batch (2) L is varied from 250 nm to 2 μm. To avoid magnetic fringe fields from the ferromagnetic electrodes, the 40-nm-thick Py electrodes (Py1, Py2) were sputter deposited first on a thermally oxidized silicon substrate. Different geometric aspect ratios of Py1 and Py2 are used to obtain different coercive fields[19]. We can thus control the relative magnetization configuration (parallel/anti-parallel) of Py1 and Py2, by sweeping an applied magnetic field **B**, directed parallel to their magnetic easy axis. The sizes of Py1 and Py2 in batch I were $2.0 \times 0.8\ \mu m^2$ and $14 \times 0.5\ \mu m^2$ respectively, as shown in Fig. 1a. An additional set of Py1 and Py2, with sizes of $2.0 \times 0.5\ \mu m^2$ and $14 \times 0.1\ \mu m^2$, was used in batch II. This set showed an improved magnetic switching behaviour and had coercive fields three times larger.

In the second fabrication step, 50-nm-thick crossed Cu strips were deposited by e-gun evaporation in 1×10^{-8} mbar vacuum. Before Cu deposition, the oxide of the Py electrodes was removed by ion milling, to ensure transparent contacts. The conductivities of the Py and Cu films were determined to be $\sigma_{Py} = 6.6 \times 10^6\ \Omega^{-1}\,m^{-1}$ and $\sigma_{Cu} = 3.5 \times 10^7\ \Omega^{-1}\,m^{-1}$ at room temperature. At 4.2 K both conductivities increased by a factor of 2.

The measurements were performed by standard a.c. lock-in techniques, using current magnitudes of 100 μA to 1 mA. We note that in the 'conventional' spin-valve geometry (sending a current I from contacts to 1 to 7, and measuring the voltage V between contacts 4 and 9), the signal $R = V/I$ was completely dominated by AMR and Hall effects of the Py contacts, having a typical magnitude of 10 mΩ. Although we have used the AMR signal of the contacts to confirm the switching of the Py electrodes, its presence has made

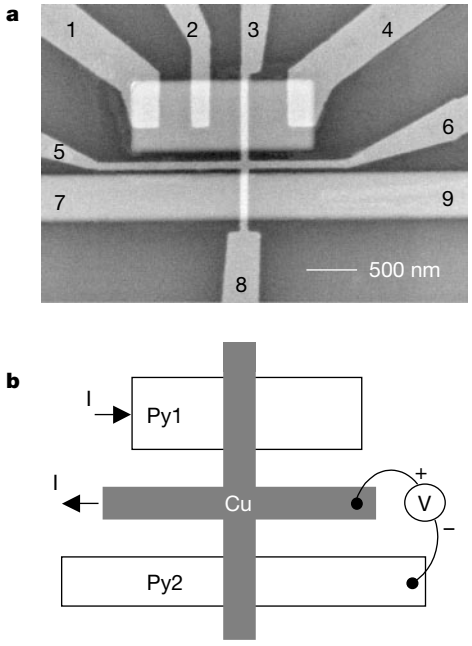

Figure 1 Sample layout. **a**, Scanning electron microscope image of the mesoscopic spin valve junction. The two wide horizontal strips are the ferromagnetic electrodes Py1 and Py2. The vertical arms of the Cu cross (contacts 3 and 8) lie on top of the Py strips; the horizontal arms of the Cu cross form contacts 5 and 6. Contacts 1, 2, 4, 7 and 9 are attached to Py1 and Py2 to allow four terminal AMR measurements of the Py electrodes. **b**, Schematic representation of the non-local measurement geometry. Current is entering from contact 1 and extracted at contact 5. The voltage is measured between contact 6 and contact 9.

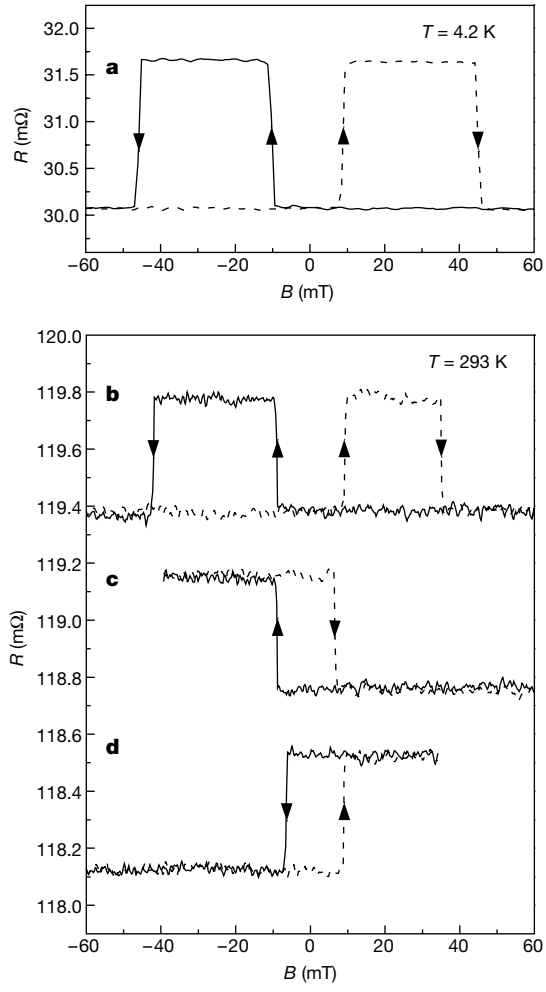

Figure 2 The spin valve effect at $T = 4.2$ K (**a**) and room temperature (**b**) in the non-local geometry for a sample with 250 nm Py electrode spacing. An increase in resistance is observed, when the magnetization configuration is changed from parallel to anti-parallel. The solid (dashed) lines correspond to the negative (positive) sweep direction. **c**, **d**, The 'memory effect'. For clarity **c** and **d** are offset downwards. We note that the vertical scale of **a** is different from that of **b**, **c** and **d**. The sizes of the Py1 and Py2 electrodes are $2.0 \times 0.5\ \mu m^2$ and $14 \times 0.1\ \mu m^2$.

any observation of a spin-valve signal in the conventional spin-valve geometry impossible.

However, in the non-local spin-valve geometry (see Fig. 1b) these spurious effects can be eliminated. This technique is similar to the "potentiometric" method of Johnson[13,14]. However, in our case, we have completely separated the current and the voltage circuits. Current now enters from contact 1 (Py1) and is extracted at contact 5 (Cu), whereas the voltage is measured between contact 6 (V_{Cu}) and contact 9 (V_{Py2}). Changing the relative magnetization configuration of Py1 and Py2 from parallel to anti-parallel will yield a signal only if the densities (electrochemical potentials) of the spin-up and spin-down electrons in the centre of the Cu cross are unequal. In a parallel configuration Py2 will measure the highest value of the two unequal spin electrochemical potentials, whereas in an anti-parallel configuration it will measure the lower value. Changing from a parallel to an anti-parallel configuration will therefore decrease the voltage (V_{Py2}) measured by Py2, resulting in an increase in the voltage difference ($V_{Cu} - V_{Py2}$) measured, and hence an increase of the resistance.

Figure 2a and b shows typical data taken at 4.2 K and room temperature for a sample from batch II, with a 250-nm Py electrode spacing. While sweeping the magnetic field from negative to positive field, we observed an increase in the resistance when the magnetization of Py1 flips at 9 mT, resulting in an anti-parallel magnetization configuration. When the magnetization of Py2 flips at 47 mT (4.2 K) and 38 mT (room temperature), the magnetizations are parallel again, but now point in the opposite direction. The magnitude of the measured background resistance, around 30 mΩ at 4.2 K and 120 mΩ at room temperature, depends on the geometrical shape of the Cu cross and is typically a fraction of the Cu square resistance.

Figure 2c and d shows the 'memory effect'. Coming from high positive **B** field, the sweep direction of the **B** field is reversed after Py1 has switched, but Py2 has not. At the moment of reversing the sweep direction, the magnetic configuration of Py1 and Py2 is anti-parallel, and accordingly a higher resistance is measured. When the **B** field is swept back to its original high positive value, the resistance remains at its increased level until Py1 switches back at a positive field of 9 mT. At zero **B** field the resistance can therefore have two distinct values, depending on the magnetic history of the Py electrodes. Samples with larger Py electrode spacing show identical switching behaviour, but the magnitude of the spin signal ΔR is reduced, as we will discuss below.

We have calculated the theoretically expected magnitude and the Py electrode distance dependence of the spin valve signal ΔR for the non-local geometry of Fig. 1b in the diffusive transport regime and for transparent interfaces, following the lines of the standard Valet Fert model for GMR[20,21], adopted for our multi-terminal geometry. We obtain[22]:

$$\Delta R = \frac{\alpha_F^2 \frac{\lambda_N}{\sigma_N A} e^{(-L/2\lambda_N)}}{(M+1)[M\sinh(L/2\lambda_N) + \cosh(L/2\lambda_N)]} \quad (1)$$

where $M = (\lambda_N\sigma_F/\lambda_F\sigma_N)(1-\alpha_F^2)$, $\alpha_F = \sigma_\uparrow - \sigma_\downarrow/\sigma_\uparrow + \sigma_\downarrow$ is the bulk current polarization of the Py electrodes, $\sigma_\uparrow$ ($\sigma_\downarrow$) are spin up (down) conductivities in the ferromagnet, σ_N (σ_F) is the total conductivity of the normal metal (ferromagnetic metal), λ_N (λ_F) is the spin-flip length in the normal metal (ferromagnetic metal), L is the distance between the two Py electrodes, and A is the cross-sectional area of the normal metal wire. Equation (1) shows that for $\lambda_N \ll L$, the magnitude of the spin signal ΔR will decay exponentially as a function of L. In the opposite limit, $\lambda_F \ll L \ll \lambda_N$, the spin signal ΔR has a $1/L$ dependence. We note that the spin signal ΔR is determined by the bulk conductances of the ferromagnet and normal metal over a distance of the spin-flip lengths. The origin of the spin signal is therefore different from the spin-dependent transport in tunnel junction experiments, where the density of states at the interface is the important quantity for the magnitude of the spin signal[23]. Hence, for tunnel junctions, the nature of the first atomic layers near the interface is crucial, whereas for transparent contacts, which is the case for our device, the interface properties are expected to be less important[15,21].

We have measured the reduction of the magnitude of spin signal ΔR as a function of the Py electrode spacing L, as shown in Fig. 3. By fitting the data to equation (1) we have obtained λ_N in the Cu wire. From the best fits we find $\lambda_N = 1 \pm 0.2\,\mu$m at $T = 4.2$ K, and $\lambda_N = 350 \pm 50$ nm at room temperature. The values of λ_N are compatible with those reported in the literature[24]: $\lambda_N \approx 450$ nm for Cu in GMR measurements at 4.2 K. However, we cannot make a straightforward comparison between the GMR results and ours. In the thin films we use, the elastic mean free path of the electrons is limited by surface scattering, causing the conductivity of the Cu to be smaller than in GMR layers. We also note that in Fig. 3 no good fit can be obtained for data where $L = 250$ nm. As the Py electrode spacing L approaches the width W of the Cu wire, the presence of the side arms (Fig. 1a) will give rise to a local enhancement of the conductance at the Cu cross and hence can result in an increase in the spin signal. Therefore, in this limit, we can expect deviations from our one-dimensional model.

We can calculate the spin-flip times τ_{sf} in the Cu wire, using a Fermi velocity of $\nu_F = 1.57 \times 10^6\,\mathrm{m\,s^{-1}}$ (ref. 25). At 4.2 K we find $\tau_{sf} = 42$ ps, while at room temperature $\tau_{sf} = 11$ ps. We will not discuss the physics of the spin-flip scattering process here. However, comparing the spin-flip time to the elastic scattering time $\tau_e = 2.9 \times 10^{-14}$ s at 4.2 K, we find that on average the spin is flipped after about 10^3 elastic scattering events in the Cu wire.

In principle the fits of Fig. 3 also yield the spin polarization α_F and the spin-flip length λ_F of the Py electrodes. However, the values of α_F and λ_F cannot be determined separately, because in the relevant limit ($M \gg 1$) which applies to our experiment ($12 \leqslant M \leqslant 26$), the spin signal ΔR is proportional to the product $\alpha_F^2\lambda_F^2$. From the fits we find $\alpha_F\lambda_F \approx 1.2$ nm at 4.2 K and $\alpha_F\lambda_F \approx 0.5$ nm at room temperature. Taking, from refs 17 and 18, a spin-flip length in the Py electrode of $\lambda_F = 5.5$ nm (at 4.2 K), a bulk current polarization of 22% in the Py electrodes at 4.2 K is obtained: $\alpha_F \approx 0.22$. These values are in the same range as the results obtained from the analysis of the GMR effect[9,10,17,18,24].

With the obtained parameters we can calculate the maximum current polarization $P = I_\uparrow - I_\downarrow/I_\uparrow + I_\downarrow$ in the Cu wire. For the samples with the smallest Py electrode spacing we obtain $P \approx 2\%$ at 4.2 K. When we scale the observed signals to the device cross-sections, we find that the scaled spin-valve signal of refs 13 and 14 is typically four orders of magnitude larger than ours. This contrast

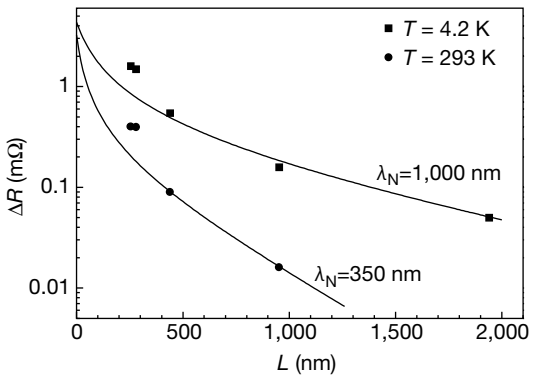

Figure 3 Dependence of the magnitude of the spin signal ΔR on the Py electrode distance L. The solid squares represent data taken at $T = 4.2$ K; the solid circles represent data taken at room temperature. The solid lines represent the best fits based on equation (1).

corresponds with the need to invoke a spin polarization of the current in the normal metal of about 100%, to explain the results of refs 13 and 14 in terms of spin accumulation. In our opinion this must imply that the observed effects of refs 13 and 14 cannot be related to spin accumulation.

We have thus demonstrated spin injection and accumulation in a mesoscopic spin valve. We find a surprisingly long spin-flip length in Cu of around 1μm at 4.2 K and about 350 nm at room temperature. For the smallest Py electrode spacing, the magnitude of the spin signal and the current polarization P in the Cu wire are limited by the unfavourable ratio of the spin-independent resistance of the Cu strips (L/σ_N) and the spin-dependent resistance of the Py ferromagnet (λ_F/σ_F). In principle, larger signals can therefore be obtained by a proper choice of materials and geometries.

Finally we note that our system permits the study of spin transport phenomena, such as controlled spin precession in solid state devices and the control of spin-polarized currents at room temperature by additional ferromagnetic contacts[3,26]. □

Received 3 November 2000; accepted 2 January 2001.

1. Prinz, G. A. Spin-polarized transport. *Phys. Today* **48,** 58–63 (1995).
2. Prinz, G. A. Magnetoelectronics. *Science* **282,** 1660–1663 (1998).
3. Brataas, A., Nazarov, Y. N. & Bauer, G. E. W. Finite-element theory of transport in ferromagnet-normal metal systems. *Phys. Rev. Lett.* **84,** 2481–2484 (2000).
4. Johnson, M. & Silsbee, R. H. Interfacial charge-spin coupling: injection and detection of spin magnetization in metals. *Phys. Rev. Lett.* **55,** 1790–1793 (1985).
5. Kikkawa, J. M. & Awschalom, D. D. Lateral drag of spin coherence in gallium arsenide. *Nature* **397,** 139–141 (1999).
6. Fiederling, R. *et al.* Injection and detection of a spin-polarized current in a light-emitting diode. *Nature* **402,** 787–790 (2000).
7. Ohno, Y. *et al.* Electrical spin injection in a ferromagnetic semiconductor heterostructure. *Nature* **402,** 790–792 (2000).
8. Malajovich, I., Kikkawa, J. M., Awschalom, D. D. Coherent transfer of spin through a semiconductor heterointerface. *Phys. Rev. Lett.* **84,** 1015–1018 (2000).
9. Gijs, M. A. M. & Bauer, G. E. W. Perpendicular giant magnetoresistance of magnetic multilayers. *Adv. Phys.* **46,** 285–445 (1997).
10. Ansermet, J.-Ph. Perpendicular transport of spin-polarized electrons through magnetic nanostructures. *J. Phys. Cond. Matter* **10,** 6027–6050 (1998).
11. Ebels, U., Radulescu, A., Henry, Y., Piraux, L. & Ounadjela, K. Spin accumulation and domain wall magnetoresistance in 35 & nm Co wires. *Phys. Rev. Lett.* **84,** 983–986 (2000).
12. Katine, J. A., Albert, F. J., Buhrmann, R. A., Myers, E. B. & Ralph, D. C. Current driven magnetization reversal and spin wave excitations in Co/Cu/Co pillars. *Phys. Rev. Lett.* **84,** 3149–3152 (2000).
13. Johnson, M. Spin accumulation in gold films. *Phys. Rev. Lett.* **70,** 2142–2145 (1993).
14. Johnson, M. Bipolar spin switch. *Science* **260,** 320–232 (1993).
15. Fert, A. & Lee, S. Theory of the bipolar spin switch. *Phys. Rev. B* **53,** 6554–6565 (1996).
16. Herschfield, S., Zhao, L. Z. Charge and spin transport through a metallic ferromagnetic-paramagnetic-ferromagnetic junction. *Phys. Rev. B* **56,** 3296–3305 (1997).
17. Steenwyk, S. D., Hsu, S. Y., Loloee, R., Bass, J. & Pratt Jr., W. P. Perpendicular-current exchanged-biased spin-valve evidence for a short spin-diffusion length in permalloy. *J. Magn. Magn. Mater.* **170,** L1–L6 (1997).
18. Dubois, S. *et al.* Evidence for a short spin diffusion length in permalloy from the giant magnetoresistance of multilayered nanowires. *Phys. Rev. B* **60,** 477–484 (1999).
19. Crangle, J. *The Magnetic Properties of Solids* Ch. 6 (Edward Arnold, London, 1977).
20. Van Son, P., van Kempen, H. & Wyder, P. Boundary resistance of the ferromagnetic-nonferromagnetic metal interface. *Phys. Rev. Lett.* **58,** 2271–2273 (1987).
21. Valet, T. & Fert, A. Theory of the perpendicular magnetoresistance in magnetic multilayers. *Phys. Rev. B* **48,** 7099–7113 (1993).
22. Filip, A. T., Hoving, B. H., Jedema, F. J. & Van Wees, B. J. Experimental search for the electrical spin injection in a semiconductor. *Phys. Rev. B* **62,** 9996–9999 (2000).
23. Meservey, R. & Tedrow, P. M. Spin-polarized electron tunneling. *Phys. Rep.* **238,** 173–243 (1994).
24. Yang, Q. *et al.* Spin flip diffusion length and giant magnetoresistance at low temperatures. *Phys. Rev. Lett.* **72,** 3274–3277 (1994).
25. Ahscroft, N. W. & Mermin, N. D. in *Solid State Physics* Ch. 2 (ed. Crane, D. G.) 38 (W. B. Saunders, Orlando, 1976).
26. Hernando, D. H., Nazarov, Yu. V., Brataas, A. & Bauer, G. E. W. Conductance modulation by spin precession in noncollinear ferromagnetic normal-metal ferromagnetic systems. *Phys. Rev. B* **62,** 5700–5712 (2000).

Acknowledgements

We thank H. Boeve, J. Das and J. de Boeck at IMEC (Belgium) for support in sample fabrication, M. S. Nijboer for experimental assistance and T. M. Klapwijk for discussions. We wish to thank the Stichting Fundamenteel Onderzoek der Materie and the EU project SPIDER for financial support.

Correspondence should be addressed to F.J.J. (e-mail: jedema@phys.rug.nl).

Shear-induced molecular precession in a hexatic Langmuir monolayer

Jordi Ignés-Mullol* & Daniel K. Schwartz*

Department of Chemistry, Tulane University, New Orleans, Louisiana 70118, USA

** Present addresses: Department de Química Física, Universitat de Barcelona, Martí i Franquès I, Barcelona E08028, Spain (J.I.-M.); Department of Chemical Engineering, University of Colorado, Boulder, Colorado 80309, USA (D.K.S.)*

Liquid crystalline behaviour is generally limited to a select group of specially designed bulk substances. By contrast, it is a common feature of simple molecular monolayers and other quasi-two-dimensional systems[1], which often possess a type of in-plane ordering that results from unbinding of dislocations—a 'hexatic' liquid crystalline phase. The flow of monolayers is closely related to molecular transport in biological membranes, affects foam and emulsion stability and is relevant to microfluidics research. For liquid crystalline phases, it is important to understand the coupling of the molecular orientation to the flow. Orientationally ordered (nematic) phases in bulk liquid crystals exhibit 'shear aligning' or 'tumbling' behaviour under shear, and are described quantitatively by Leslie–Ericksen theory[2]. For hexatic monolayers, the effects of flow have been inferred from textures of Langmuir–Blodgett films[3–5] and directly observed at the macroscopic level[6–10]. However, there is no accepted model of hexatic flow at the molecular level. Here we report observations of a hexatic Langmuir monolayer that reveal continuous, shear-induced molecular precession, interrupted by occasional jump discontinuities. Although superficially similar to tumbling in a bulk nematic phase, the kinematic details are quite different and provide a possible mechanism for domain coarsening and eventual molecular alignment in monolayers. We explain the precession and jumps within a quantitative framework that involves coupling of molecular orientation to the local molecular hexatic 'lattice', which is continuously deformed by shear.

The interfacial thermodynamics and rheology of molecular films like Langmuir monolayers are responsible for the stability of multiphase materials such as foams and emulsions[11]. They are important model systems for studies of dynamics and molecular interactions in bio-membranes and, as quasi-two-dimensional systems, display a variety of unusual liquid crystalline phenomena. The application of synchrotron X-ray scattering and specialized imaging techniques such as fluorescence and Brewster angle microscopy (BAM) have

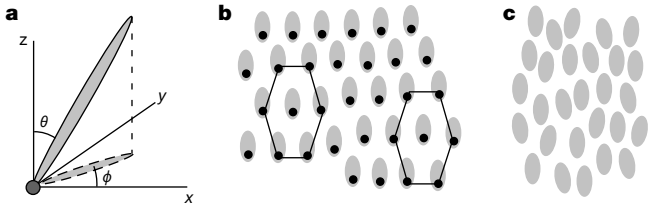

Figure 1 Hexatic and nematic phase representations. **a**, A cartoon showing the molecular geometry of rod-shaped molecules in a tilted hexatic phase. The molecule is tilted away from the surface normal by the angle θ, and the azimuthal direction of tilt is given by the angle φ. **b**, Schematic picture of a tilted hexatic phase viewed from above. The projection of the molecules on the surface plane are oval; the dark circles represent the headgroups at the interface. In this case, the molecular tilt direction is locked into the nearest neighbour direction of the local distorted-hexagonal unit cell. We note that the orientation of the unit cell remains uniform despite the presence of a lattice dislocation that destroys the positional registry of the lattice. **c**, Schematic picture of a nematic phase. Molecules are aligned in a common direction on average, but their positions are random.